Contextual Anomaly Detection Cueing Methods for Hyperspectral Target Recognition

Kelly D. Friesen, Trevor J. Bihl, Kenneth W. Bauer, Mark A. Friend
Department of Operational Sciences, Air Force Institute of Technology, Wright Patterson AFB, OH, USA

Abstract – Detection and recognition are two primary tasks of hyperspectral imaging, with the objective of detecting and identifying materials remotely. Frequently these are done separately, with anomaly detection or signature recognition being applied, but not both in conjunction. Here, we introduce a fully automatic hyperspectral-based target recognition system through the combination of automatic anomaly detection, anomaly segmentation, pixel cueing methods for background reduction filtering, signature matching, automatic atmospheric compensation, and vegetation index thresholding for automatic atmospheric compensation. Of interest herein are the handling of pixels and groupings of pixels detected as a statistical anomaly; various methods of processing anomaly groups are examined. Results are provided using HYDICE hyperspectral radiance images and collected ground reflectance data.

Key Words – ATD, ATR, Automatic Target Recognition, Automatic Target Detection, chipping, cluster identification, cueing, hyperspectral, remote sensing.

I. Introduction

Hyperspectral imaging (HSI) systems are a form of imaging spectroscopy, collecting both spatial and spectral features; in essence HSI operates as a panchromatic sensor with individual spectrometers for each pixel [1]-[3]. Other modalities, such as multispectral imaging (MSI) cover a large portion of the spectrum; however MSI bands are collected with coarse spectral sampling [2], whereas HSI has a multitude of finely sampled spectral bands. Fine spectral sampling enables measurement of minute spectrally reflected and/or emitted features, offering the potential to remotely detect, examine, and identify materials through differing spectral characteristics. In operation, HSI sensors collect spectral characteristics sequentially, building a three dimensional image object known as an image cube. In such an image cube, notionally, the *x* and *y* axes contain spatial information, while the *z* axis contains spectral data. HSI sees frequent application for three primary purposes: anomaly detection, change detection, and spectral signature matching [1]. The research herein focuses on a combination of anomaly detection and spectral signature matching. Automatic anomaly detection (ATD) seeks pixels significantly different than the rest of the image; in contrast automatic target recognition (ATR) involves spectral signature matching to identify spectral similarity of a pixel to a known material.

Applications of cueing in ATD and ATR frequently include focusing an analyst's attention to a particular pixel or location; an example of automatic HSI ATD cueing includes the search and rescue operations of the Civil Air Patrol's ARCHER program [1]. Cueing methods such as this require a 'user in the loop,' and are naturally susceptible to collecting more data than can be analyzed, confirmation bias [4] and/or operator fatigue [5]; such situations can lead to a preponderance of data, yet lack of information [6]. As a variant, cueing in this paper refers to algorithm cueing, where signature matching algorithms are cued to process detected anomalies. The outcome of this autonomous method, Fig. 1 [7], would then be sent to an analyst. Some of the methods leading from ATD cues to recognition involve combining multiple spectra for a detected anomaly; this is akin to combining multiple vegetation spectra for atmospheric compensation.

Ratches [8] offered a similar generic path from input to detection to classification; however a methodology was not detailed. Chang and Chiang [9] developed an anomaly classification method based on detected statistical anomalies; however, this classification scheme was based on in-scene classes with anomalous points clustered based on statistics.

The methodology presented in Fig. 1 incorporates modules facilitating the testing of various functions and combinations, with Step 0, loading image and ground truth data, and Step 1a being automatic atmospheric compensation. Anomaly detection, Step 1b in Fig. 1, is applied as a background reduction filter to identify probable objects of interest while discarding apparent background; such a method was applied by Manolakis et al. [10] for improved signature matching. The identified anomalous pixels and groups of pixels are then classified in Step 2,

Corresponding Author: Trevor J. Bihl, Email: Trevor.Bihl@afit.edu

through established signature matching algorithms. Although the algorithms used in this study are from the literature, the end-to-end automation, flexibility of changing algorithms, vegetation thresholding method for automatic atmospheric compensation, and the method for selecting and grouping detected anomalies

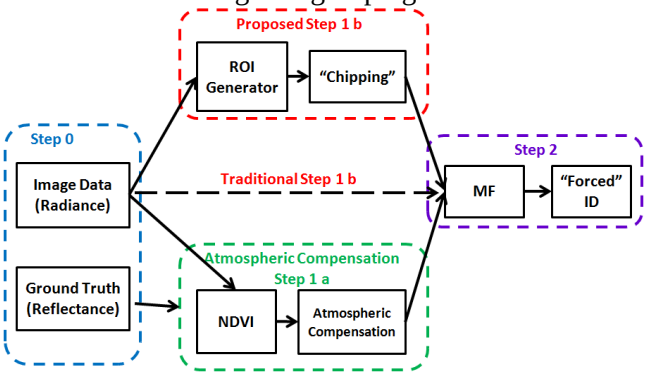

Fig. 1 Automated methodology

for signature matching are unique.

In HSI ATD, anomalies can consist of individual pixels or groupings of pixels. In this research, particular attention is given to reducing the number of points under consideration in ATR by first processing the image with an ATD algorithm. Comparisons of applying matched filters to the entire image to various means of using an anomaly detector for background reduction, removing statistical background information are provided. Emphasis is given to automating the entire process, with a minimum amount of user input.

This paper is organized as follows: Section II reviews HSI, characteristics of the data, and dimensionality reduction for creating a parsimonious dataset for analysis. Section III describes the automatic atmospheric compensation applied, while Section IV describes automatic target detection. Section V describes signature matching and aspects of the combined methodologies presented in Fig. 1. Concluding remarks and discussions appear in Section VI.

II. Hyperspectral Remote Sensing

The HSI images used herein, Fig 2, are from the Forest I and Desert II Radiance collections from the HYDICE pushbroom sensor; these images provide radiance data for 210 bands with 10nm spectral sampling over 400 – 2500 nm, thereby covering the visible, NIR and short wave infrared regions [3] [11]. The images used for this research were both collected at approximately 5,000' AGL.

Provided with the Forest I and Desert II radiance images are 5nm spectrally sampled field spectrometer reflectance measurement files for in-scene objects and background. For modeling vegetation, reflectance data for in-scene sweet gum trees and creosote bushes were used respectively for the Forest and Desert images. Known man-made objects of interest total: 10 in the Desert and 21 in the Forest image. In this study, one object class of interest was selected for each image, with 223 and 348 target pixels respectively provided within the Forest and Desert images; yielding percentages of 0.18% (Forest) and 0.309% (Desert) of total pixels being known in-scene target pixels.

Fig. 2 Images used in analysis. the image on the left will be referred to as Forest (611 by 201 spatial pixels); the image on right (401 by 281 spatial pixels) as Desert.

2.1 Dimensionality Reduction

Fringe bands (at the edges of the spectral regions), bands associated with water absorption, and noise filled bands were identified (bands 1-9, 98-114, 133-157, 201-210) and discarded in similar fashion as in Johnson [15] and Farrell and Marsereau [16], resulting in 149 bands available for analysis. Although discarding said bands removed 61 bands from the HYDICE images (29% of the image), there is not necessarily a parsimonious dataset present. To reduce dimensionality further for efficiency in a computational sense while preserving variability (in this case energy measured), Principal Component Analysis (PCA) was used.

PCA is frequently applied to HSI due to its straightforward and predictable behavior [3][16]-[18]. PCA preserves and groups a maximal amount of variance through a linear transformation of data, using the eigenvectors of the data correlation matrix [19]. Principal component (PC) bands are orthogonal to each other, with the first PC containing the most variance, the second PC the second most variance and

so forth [19]. In terms of dimensionality assessment, the cumulative variance explained and the magnitudes of the image covariance matrix eigenvalues through a Scree plot are often used [19]. For the Forest image, 10 PC bands were retained, equivalent to 99.85% of the variance in the HSI image cube; similarly for the Desert image, 10 PC bands were retained preserving 99.78% of the variance in the image.

2.2 Normalized Difference Vegetation Index (NDVI)

Due to the presence of water, chlorophyll, and other pigments, vegetation typically appears green in visible wavelengths due to light absorption properties; also, between 700nm and 1300nm vegetation typically acts as a scatterer, causing vegetation to appear bright [3][12][13]. Linear vegetation indices take advantage of this property, measuring the slope between the absorbed visible light and the mostly reflected NIR light with high values corresponding to probable vegetation. One method, NDVI, developed by Rouse et al. [14], detects instances of probable vegetation using red and NIR bands. NDVI is regarded as having a high dynamic range and sensitivity to changes in vegetation cover [12]; it is described by a linear relationship

$$NDVI = \frac{L(NIR) - L(Red)}{L(NIR) + L(Red)}, \quad (1)$$

where *L* refers to radiance at selected *NIR* and *Red* wavelengths bands, respectively [1][12][14]. Scores for NDVI vary from -1 to 1, the higher magnitudes typically being associated with probable vegetation.

III. Atmospheric Compensation for ATR

Remotely measured HSI pixels inherently include additional effects from external sources, requiring radiative transfer considerations [1]-[3]; included in radiance images are atmospheric influences, weather effects, illumination, path radiance, and adjacency aspects, among others [1][12][23]. However, for signature matching known materials are frequently analyzed by collecting reflectances, a unitless ratio of the amount of light reflected to light striking an object, requiring a known source and controlled conditions [12]. Atmospheric compensation, Step 1a in Fig. 1, is therefore a necessity when searching for a known signal collected using ground equipment to convert ground measurements of reflectance to the same unit space as angle per area [1][3][12][23].

Methods of atmospheric compensation frequently rely on *a priori* knowledge in the form of a known target being in-scene for reference, as in Empirical Line Methods, or appropriate parameter selection for model based approaches. In a purely automatic system, such approaches are not appropriate and therefore the vegetation normalization (VN) method, which leverages vegetation detection, was used [1][3]. While VN is considered to offer poor quality results [3], an advantage is achieved in the ease of automation. The VN approach used herein applies a linear conversion from reflectance to radiance employing in-scene pixels estimated to be vegetation with appropriately selected known reflectance data for vegetation. The linear relationship between estimated pupil-plane radiance and reflectance employs equation (2),

$$\hat{L}(\lambda) = \hat{a}(\lambda)\rho(\lambda) + \hat{b}(\lambda), \quad (2)$$

where $\hat{a}$ is a linearly computed gain vector, $\hat{b}$ is a linearly computed offset vector, with $\hat{L}$ the estimated pupil-plane radiance of the given reflectance spectra vector, ρ, each as a function of wavelength λ [1][3]. The gain and offset were calculated through linear relationships, with

$$\hat{a}(\lambda) = \frac{L_2(\lambda) - L_1(\lambda)}{\rho_2(\lambda) - \rho_1(\lambda)} \quad (3)$$

and

$$\hat{b}(\lambda) = \frac{L_1(\lambda)\rho_2(\lambda) - L_2(\lambda)\rho_1(\lambda)}{\rho_2(\lambda) - \rho_1(\lambda)} \quad (4)$$

where the subscripts 1 and 2 indicating appropriately corresponding radiance and reflectance data sources [1][3].

3.1 Vegetation Index Thresholding

Due to a desire to have consistent operating points among different types of images, raw NDVI thresholds for VN are possibly inappropriate given differing distributions of vegetation across environments and scenery types, an NDVI score associated with a forest image would possibly result in few if any pixels being selected as vegetation in a desert image. An alternative method of selecting a percentage bound of the total pixels to be considered as vegetation was adopted. As an example of the use, this research selects 1% of the top scoring NDVI values for retention as vegetation; this operating point equates to 1,228 points for the forest image and 1,126 points for the desert image. Pixels corresponding to these scores are then averaged for all bands to create the reference VN vegetation radiance vector.

3.2 Atmospheric Compensation Data Points

For both images equations (2)-(4) were computed by selecting appropriate vectors. For both images, ρ_1

was a vector of zeros corresponding to an ideal dark reflectance vector; correspondingly, L_1 was a constructed vector of the darkest radiance in the image, created by taking the minimum value in each wavelength [3]. For both images, L_2 vectors were computed through the *Vegetation Index Thresholding* approach using the mean vegetation radiance vector. For the Forest image, data for the ρ_2 vector was taken from radiance information from in-scene Sweet Gum Trees; whereas for the Desert image the ρ_2 vector was created using reflectance data from in-scene Creosote brush.

IV. Anomaly Detection

Anomaly detection in HSI involves a statistical classification problem where pixels different from the background are detected; detectors apply either global or local background models with varying advantages to each [1][3][25]. The RX algorithm is a sliding window approach to anomaly detection where the local, within window, statistics are examined for anomalies [1][3][24]-[26]. RX is an extension of generalized likelihood ratio test and approximates to a Mahalanobis distance for large numbers of points in an image [1][24]-[26]. RX is expressed as

$$RX(x) = (\mathrm{x} - \hat{\mu})^T \hat{\mathrm{C}}^{-1} (\mathrm{x} - \hat{\mu}), \quad (5)$$

with

$$\hat{\mathrm{C}} = \left(\left(\frac{\mathrm{N}}{\mathrm{N}+1} \right) \hat{\Sigma} + \left(\frac{1}{\mathrm{N}+1} \right) (\mathrm{x} - \hat{\mu})(\mathrm{x} - \hat{\mu})^{\mathrm{T}} \right), \quad (6)$$

where x is a given pixel vector at the center of the window; $\hat{\mu}$, the estimated mean vector of pixels in the window; N, the number of pixels in the window; and $\hat{\Sigma}$, the estimate of the window's covariance matrix [3]. As N becomes large, $\hat{\mathrm{C}}$ converges to $\hat{\Sigma}$, and equation (5) converges to the Mahalanobis distance between the pixel vector and the mean vector of the window [26].

For anomaly detection, pixels with an RX score greater than the chi-squared distribution, $\chi^2_{\alpha,(\mathrm{N}-1)}$, are viewed as anomalous. RX was selected for the "ROI [Region of Interest] Generator" in Step 1b of Fig. 1, due to its ubiquity, simple mathematical expression, and known expectations of performance.

Performance of ATD algorithms are typically displayed through Receiver Operating Characteristic (ROC) curves [3]; ROC curves plot false positives on the x-axis and true positives on the y-axis [27]; thresholds for the ROC curve are from varying the significance level of the chi-squared distribution of the RX scores. Presented in Fig. 3 are ROC curves for the RX algorithm when applied to the two images in Fig. 2.

For the Forest and Desert images, selecting appropriate criteria for operating points from the RX detected anomalies is critical. In operation, knowledge of true positives and false positives would not be known a priori. For the example herein, an operating point with 20% false positives was selected (equating to a Chi-squared distribution setting of 0.378 for both images); although this enables many false positives to be included, the combined ATD background reduction to cue to ATR mitigates this. This operating point resulted in 11.84% of the Forest and 11.19% of the

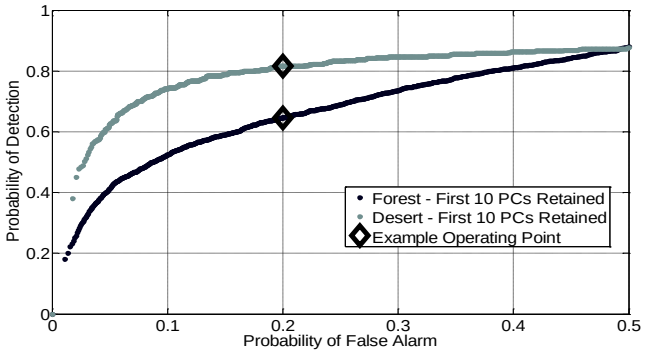

Fig. 3 Anomaly Detection ROC Curves for Forest and Desert Images using known man-made objects in-scene. The true and false positive fractions equating to a Chi squared distribution setting of 0.378 is indicated by the diamond.

Desert image identified as anomalous, with false negatives of 14.35% for the target class in the forest image and 21.55% in the desert image (which must be considered when discussing final performance).

4.1 Background Filtering/ROI Chipping

Chipping frequently refers to selecting a region around a detected anomaly for user viewing and analysis [1]. In this research, "Chipping" relates to grouping detected anomalies from the ATR process through various means, listed in Table 1, for background filtering as an additional automatic computational classification in Step 1b in Fig. 1. Through automatic target detection preprocessing/background filtering, only pixels statistically different from the background are further examined for signature matching purposes, thereby decreasing the likelihood that background pixels are grouped as possible matches for a given signature. Subsequently, detected anomalies are grouped by the five different methods presented in Table 1, offering different types of ROI clusters for evaluation. The various chipping methods listed in Table 1 permit examination of how clusters of detected anomalies relate to identifying anomalies; cluster groups are defined herein as groupings of pixels contiguously

Table 1 ROI chipping methods for background filtering

Chipping Method*	ROI Description
Averaged	Matched filter scores for pixels are averaged per group
Baseline/None	No chipping is applied, the entire image is processed for spectral similarity to a known sample
Centroid	Pixel vector of the centroid from multi-pixel anomalies used
Individual	Each ATD filtered anomalous pixel is individually examined
Majority	All pixels in a group analyzed, with score fusion used to label anomaly group identity
Mean	Averaged radiance signature from multi-pixel groups
Median	Median spectral band created from median value of each wavelength for a multi-pixel anomalies
Mode	Mode radiance band taken from a multi-pixel anomalies

*All methods are equivalent for a one pixel detected anomaly

Table 2 Example ROI chips by image for chipping methods

Chipping Method	Forest Image		Desert Image	
	Number of Chips	Avg Number of Pixels/Chip	Number of Chips	Avg Number of Pixels/Chip
Baseline/None	122,811	1	112,681	1
Individual	14,537	1	12,620	1
All Other ChippingMethods	3,547	4.098	2,707	4.662

connected to each other, diagonally connected points are also considered contiguous.

Conceptually, the chipping methods take groupings of points identified as anomalous, create matrices of each group's pixel vectors; in essence this is akin to creating vegetation spectrum in VN, only now we are creating multiple anomalous grouping spectrums. Descriptively, the *centroid* chipping method selects only the spectral from the geometric centroid of an anomaly group, a caveat being this may or may not be a pixel within the group itself; the *individual* method processes each ATD anomalous pixel and computes a matching score individually for each pixel; the *averaged* method extended the *individual* method by computing a mean matched filter score for grouped pixels, thereby incorporating some contextual knowledge of adjacent points; the *majority* method computes the spectral similarity of each pixel in a group then applying a majority voting score for the declaration of the group as the class of interest or as background; the *mean* chipping method averages the spectral signature of all pixels in a group; the *median* chipping method computes a median pupil-plane radiance of all pixels in a group; the *mode* method computes a mode pupil-plane radiance of all pixels in a group. Of note, all chipping methods are equivalent for single pixel detections. For comparison to operating with no background filtering, the *baseline* method processes the entire image through the ATR. In other words, *baseline* follows the "Traditional Step 1b" in Fig. 1.

Table 2 lists details for each HSI image and the chipping type; the absence of chipping was considered as the baseline method. The *individual* method results in much fewer pixels (7.4-7.6% of the image) to process than the baseline, however this method ignores any contextual knowledge of groupings of anomalies, in essence making each pixel its own chip; *all other chipping* methods considers the same number of chips, however the manner in which each method incorporates and handles the chips differs and the number of chips to process is considerably lower than the baseline or individual methods.

V. Automatic Target Recognition

ATR in this paper employs the commonly used Match Filter (MF) algorithm which produces similarity scores as a function of the distances between candidate target signatures and known target signatures. Higher MF scores indicate a closer match between candidate signatures and a known source. In HSI, ATR methods are frequently employed for material identification where fine spectral sampling enables detection of fine spectral features at the molecular level [3].

The baseline algorithm employed for ATR was the MF described by

$$y = \frac{(s-\hat{\mu})^T \widehat{\Sigma}^{-1} (\mathrm{x}-\hat{\mu})}{(s-\hat{\mu})^T \widehat{\Sigma}^{-1} (\mathrm{s}-\hat{\mu})}, \qquad (7)$$

where the MF score, y, results from examining each pixel vector, x; the mean vector of the image, $\hat{\mu}$; the known spectral source vector, s; and estimated covariance of the entire image, $\widehat{\Sigma}$ [1][28]. In processing equation 7, higher magnitude scores are viewed to be closer to the known spectral source than lower scores. For the chipping methods applied herein,

the Adaptive MF (AMF) was used as developed by Manolakis et al. [10].

The *baseline* method can also be termed 'none' as no chipping methods are applied, this method processes the entire image pixel by pixel using equation 7; many applications in literature (e.g. [1][3][29]) examined entire images in this manner, supporting the contention of this as the typical HSI ATR methodology, hence the term baseline. Whereas the baseline methodology assumes that no preprocessing has been performed, the combined methodology of automatic HSI anomaly detection cueing involves examining only the ATD detected anomalous pixels and groupings of pixels. When applying the AMF to the chipping methods, determining appropriate selections of AMF parameters was critical. For all chipping methods, the inverse

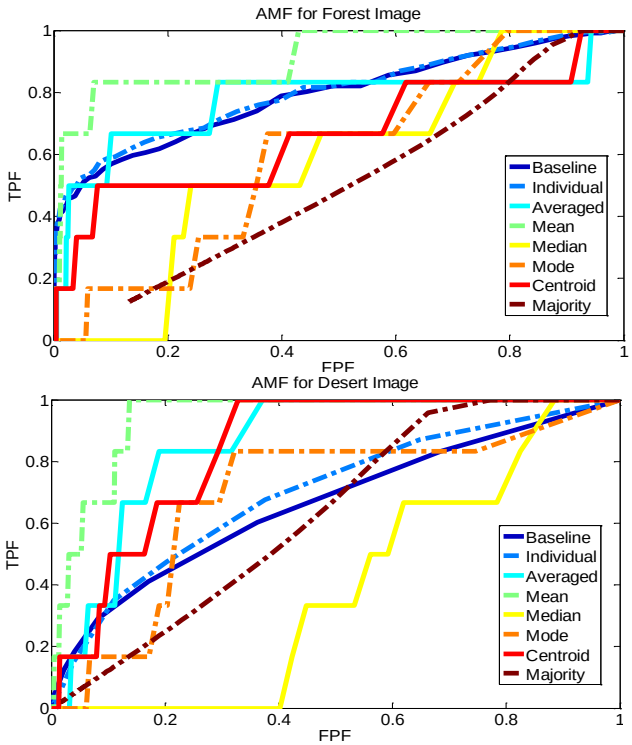

Fig. 4 Top: AMF ROC for the Forest image; Bottom: AMF ROC for the Desert image

covariance matrix and mean vector were computed using the entire image.

Fig. 4 displays ROC performance results of the chipping methods for ATR in comparison with the baseline; no initial biases were incorporated for the chipping methods due to the ATD operating point selected, Fig. 3, containing a majority of the target class and missing no whole targets (of primary importance when detecting and classifying targets). Of note, the *individual* chipping method offers similar ATR performance for both the Forest and Desert images as examining the entire image. The *mean* and *averaged* chipping methods offered consistently better ATR performance than the baseline; the *mode* and *centroid* method offered erratic performance being among the highest performing chipping methods in the Desert image and among the lowest in the Forest image. Whereas the *median* and *majority vote* methods were seen to offer the lowest performance among the methods examined. A caveat in considering the *majority vote* method must be discussed; there are four true clusters in the Forest image and six true clusters in the Desert image. This introduces the possibility that the low performance was a factor of a low number of true class clusters being present in the images.

VI. Conclusion

This research introduced an autonomous framework for HSI ATR through the incorporation of ATD background reduction filtering, automated atmospheric compensation, vegetation index thresholding, and variations on chipping. Results were provided using HYDICE HSI radiance images and collected ground reflectance data. The advantages of this framework are its conceptual simplicity and reduction in number of pixels processed by signature matching schemes when compared to computationally intensive methods.

The chipping methods in one sense could be viewed as increasing pixel mixing, on another hand decreasing the number of pixels to be processed at the expense of possibly decreasing signature matching performance. Advantages over the baseline were evident in many methods. While the performance of the individual method was similar to analyzing the whole image significant reduction in the number of points to analyze increases the list of possible methods when computation times are critical.

While, in operation, one would not have the luxury of knowing true performance of the ATD method, methods are available for robustly finding HSI ATD operating points prior to fielding [30]. One noticeable benefit of the chipping methods is their analysis of much fewer data points for ATR processing; this could be exploited as a benefit through algorithmic fusion of multiple ATR methods and/or more computationally intensive methods thereby leveraging the benefits of a computationally simple ATD background reduction to remove probable background points.

ACKNOWLEDGEMENT

This work was supported in part by the U.S. Secretary of the Air Force Department. The views expressed herein are those of the authors and are not official positions of the USAF.

REFERENCES

[1] M. T. Eismann, A. D. Stocker, and N. M. Nasrabadi, "Automated hyperspectral cueing for civilian search and rescue," Proc. IEEE, vol 97, no. 6, June 2009, pp. 1031-1055

[2] J. N. Rinker, "Hyperspectral imagery – what is it? – what can it do?" USACE 7th Remote Sensing Symposium, Portland, OR, May 1990

[3] M. T. Eismann, Hyperspectral Remote Sensing, SPIE Press, Apr. 2012

[4] P. Lehner, L. Adelman, R. DiStasio, M. Erie, J. Mittel, and S. Olson. (2008 Jan. 8) "Confirmation bias in the Analysis of Remote Sensing Data." Mitre Corporation, Rep. 06-1288. Accessed: Jan. 25, 2012, Available: http://www.mitre.org/work/tech_papers/tech_papers_07/06_1288/

[5] M. C. Mettel, "A GIS model for the determination of wetland mitigation sites," in Application of Geographic Information Systems in Hydrology and Water Resources Management, K. Kovar and H. P. Nachtnebel, Eds., IAHS Press, 1996, pp. 331-340

[6] S. Magnuson, "Military's swimming in sensor and drowning in data," National Defense Magazine, January, 2010

[7] K. D. Friesen, Automatic Target Recognition for Hyperspectral Imagery, MS Thesis, Air Force Institute of Technology, 2012

[8] J. A. Ratches, "Review of current aided/automatic target acquisition technology for military acquisition tasks," Optical Engineering, vol. 50, no. 7, July 2011

[9] C. I. Chang, and S. S. Chiang, "Anomaly detection and classification for hyperspectral imagery," IEEE Trans. Geoscience and Remote Sensing, vol. 40, no. 6, June 2002, pp. 1314-1325

[10] D. Manolakis, R. Lockwood, T. Cooley, and J. Jacobson, "Is there a best hyperspectral detection algorithm?" Proc. SPIE Algorithms and Technologies for Multispectral, Hyperspectral, and Ultraspectral Imagery XV, vol. 7334, 2009, pp. 1-16

[11] L. J. Rickard, R. Basedow, E. Zalewski, E., and P. Silverglate, P., "HYDICE: An airborne system for hyperspectral imaging," Proceedings of the SPIE , vol. 1937, 1993, pp. 173-179

[12] T. W. Ray. (1994 Oct. 13) "A FAQ on vegetation in remote sensing," Accessed: Jan. 10, 2010, Available: http://www.yale.edu/ceo /Documentation/rsvegfaq.html

[13] P. K. Connor, and D. W. Mooneyhan, "Practical applications of Landsat data," in Monitoring Earth's Ocean, Land, and Atmosphere from Space – Sensors, Systems, and Applications, A. Schnapf, Ed., AIAA, 1985, pp. 371-396

[14] J. W. Rouse, R. H. Haas, J. A. Schell, and D. W. Deering, "Monitoring vegetation systems in the great plains with ERTS," 3rd ERTS Symposium, NASA SP-351, vol. 1, 1973, pp. 309-317

[15] R. J. Johnson, Improved Feature Extraction, Feature Selection, and Identification Techniques that Create a Fast Unsupervised Hyperspectral Target Detection Algorithm, MS Thesis, Air Force Institute of Technology, Mar. 2008

[16] M. D. Farrell, and R. M. Mersereau, "On the impact of PCA dimensionality reduction for hyperspectral detection of difficult targets," IEEE Geoscience and Remote Sensing Letters, vol. 2, no. 2, Apr. 2005, pp. 192-195

[17] C. Rodarmel, and J. Shan, "Principal component analysis for hyperspectral image classification," Surveying and Land Information Systems, vol 62, no. 2, 2002, pp. 115-123

[18] D. A. Landgrebe, Signal Theory Methods in Multispectral Remote Sensing, Wiley-Interscience, New Jersey, 2003

[19] W. R. Dillon, and M. Goldstein, Multivariate Analysis: Methods and Applications, John Wiley & Sons, New York, 1984

[20] I. E. Bell, and G. V. G. Baranoski, "Reducing the dimensionality of plant spectral databases," IEEE Trans. Geoscience and Remote Sensing, vol. 42, no. 3, Mar. 2004, pp. 570-576

[21] F. Tsai, E. K. Lin, and K. Yoshino, "Spectrally segmented principal component analysis of hyperspectral imagery for mapping invasive plant species," Int'l J. Remote Sensing, vol. 28, no. 5, Mar. 10, 2007, pp. 1023-1039

[22] D. H. K. Fairbanks, and K. C. McGwire, "Patterns of floristic richness in vegetation communities of California: regional scale analysis with multi-temporal NDVI," Global Ecol. Biogeogr., vol. 13, 2004, pp. 221-235

[23] C. C. Borel, (2010) "Vegetative canopy parameter retrieval using 8-band data," DigitalGlobe 8-Band Research Challenge, Available: http://www.exelisvis.com/portals/0/pdfs/envi/8_bands_Christoph_Borel.pdf

[24] I. S. Reed, and X. Yu, "Adaptive multiple-band CFAR detection of an optical pattern with unknown spectral distribution," IEEE Trans. Acoust., Speech, Signal Process., vol 38, 1990, pp. 1760-1770

[25] D. W. J. Stein, S. G. Beaven, L. E. Hoff, E. M. Winter, A. P. Schaum, and A. D. Stocker, "Anomaly detection from hyperspectral imagery," IEEE Sig. Proc. Mag., Jan. 2002, pp. 58-69

[26] T. E. Smetek, Hyperspectral Imagery Target Detection Using Improved Anomaly Detection and Signature Matching, PhD Dissertation, Air Force Institute of Technology, June 2007

[27] T. Fawcett, (2003) "ROC graphs: notes and practical considerations for data mining researchers," Technical Report HPL-2003–4, HP Laboratories, Palo Alto, CA.

[28] D. Manolakis, and G. Shaw, “Detection algorithms for hyperspectral imaging applications,” IEEE Sig. Proc. Mag., Jan. 2002, pp. 29-43.
[29] L. Wood, Survey of ERIM approaches applicable to semi-automatic target detection and cueing for multispectral and multisensory exploitation, Technical Report: 215400-1-F, July 25, 1989.
[30] F. M. Mindrup, M. A. Friend, K. W. Bauer, “Selecting training and test images for optimized anomaly detection algorithms in hyperspectral imagery through robust parameter design,” Proceedings of SPIE, vol. 8048, pp. 80480C-80480C-15, 2011.